Cyclic stress–strain behavior of conventional grain and ultrafine grain nickel under biaxial straining

N.R. Batane, D.J. Morrison* and J.C. Moosbrugger

Results are presented on the effects of biaxial straining on the cyclic stress–strain response of ultrafine grain nickel (grain size ≈ 260 nm) and conventional grain nickel (grain size ≈ 50 μm) over a range of effective plastic strain amplitudes from 1×10^{-4} to 1×10^{-3}. Grain refinement causes an increase in saturation stress. For conventional grain nickel, non-proportional straining causes higher saturation stress than proportional straining; but the ultrafine grain material exhibits the opposite behavior.

The demonstrated ability to significantly enhance mechanical properties such as hardness and tensile strength through grain refinement has caused a great deal of interest in characterizing the fundamental mechanical behavior of nanocrystalline and ultrafine grain materials. Nanocrystalline materials are generally considered to have grain sizes less than 250 nm, while ultrafine grain materials have grain sizes between 250 and 1000 nm [1]. Several detailed reviews of the processing methods and mechanical properties of these types of materials have been published recently [1–3].

Previous experimental work on the cyclic response of nanocrystalline and ultrafine grain materials has been accomplished under uniaxial loading conditions. While there are a number of methods that are used to produce nanocrystalline and ultrafine grain materials [1], most of the uniaxial cyclic deformation studies have been on materials produced by severe plastic deformation processes [4–9] or electrodeposition [10–13]. Although these processing routes certainly cause different substructures and internal stress states, there are similarities in their responses to uniaxial cyclic deformation. Compared with conventional grain size materials, nanocrystalline and ultrafine grain materials exhibit reduced resistance to strain-controlled low cycle fatigue [5,7,9], enhanced resistance to stress-controlled high cycle fatigue [6–8,10,13] and significantly higher cyclic saturation stresses [4–

6,9,11,12]. In the present work, preliminary results on the biaxial cyclic stress–strain response of conventional grain nickel and ultrafine grain nickel are presented.

Ultrafine grain (UFG) nickel tubes were electroformed in a nickel sulfamate solution using the Barrett process with chemicals supplied by MacDermid, Inc. The bath contained 412 ml of nickel sulfamate solution (SNR-24), 44 g of boric acid, 2.6 ml of SNAP AM and 4 g of Additive A. Constant bath conditions were maintained at 60 °C and pH of 5.5 ± 0.5. Nickel-270 (99.98 wt.% Ni) was used as the anode, and an 80 mm long copper tube with a 10 mm outside diameter was used as the cathode. Approximately 3 mm of nickel was electrodeposited onto the outer surface of the copper tube. A constant current density of 0.05 A cm^{-2} was maintained by gradually increasing the plating current as the diameter of the deposit increased. After the electroplating process was completed, the copper tube was bored from the electrodeposited nickel leaving an 80 mm long nickel tube with an inside diameter of 10 mm and outside diameter of 16 mm. The inside of the nickel tube was then honed to produce a smooth inner surface. The tube was then machined into a thin-walled axial–torsional specimen having a total length of 80 mm, grip section outside diameter of 15 mm, gage section outside diameter of 12.15 mm, gage section wall thickness of 1 mm and gage section length of 15 mm. Transmission electron microscopy revealed that the grain size measured on a section perpendicular to the growth direction was normally distributed with a mean of 260 nm and standard deviation of 105 nm. X-ray diffraction indicated a strong ⟨100⟩ texture in the

* Corresponding author. Tel.: +1 315 268 6585; fax: +1 315 268 6695; e-mail: dmorriso@clarkson.edu

growth direction, which corresponds to the radial direction of the tube. The purity of the UFG nickel was about 99.9 wt.% Ni as measured using glow discharge mass spectroscopy and combustion analysis. Major impurity elements were Fe(0.065 wt.%), Cr(0.0085 wt.%), S(0.0075 wt.%), Cd(0.0040 wt.%) and C(0.0015 wt.%). Hydrogen was not detectable using these techniques, but typical values for electrodeposited nickel are on the order of 0.01 wt.% [11]. Density measurements made using Archimedes' principle indicated that the UFG nickel attained at least 99% theoretical density. The average hardness in the gage section of the UFG nickel was 217 HV.

Conventional grain (CG) nickel specimens were machined from a 19 mm diameter Ni-270 rod. The purity of the CG material was 99.98 wt.% Ni, with major impurities being C (0.0065 wt.%), Fe (0.0019 wt.%) and S (0.0001 wt.%). The dimensions of the CG nickel axial–torsional specimens were identical to those of UFG specimens described above. After machining, the CG nickel specimens were annealed in a vacuum furnace at 500 °C for 1 h to achieve a grain size of about 50 μm. A weak $\langle 111 \rangle$ texture in the longitudinal direction was noted in the CG material. The average hardness in the gage section of the annealed CG nickel was 96 HV.

All specimens were hand ground using successively finer grits of silicon carbide paper and then electropolished in a solution of 100 ml perchloric acid and 400 ml ethanol. Optimum electropolishing results were obtained at 50 V and −50 °C.

Axial–torsional cyclic deformation experiments were performed at room temperature on an MTS axial–torsional testing system under total strain-controlled conditions using a sinusoidal command signal. Axial and shear total strain amplitudes were continuously adjusted to achieve the target nominal plastic strain amplitudes. The axial–torsional tests were carried out under both proportional and 90° out-of-phase non-proportional straining. These tests will be referred to as proportional and non-proportional tests. An automated MTS Test-Ware-SX program was used to control the test parameters and to digitally acquire data at specified intervals. An MTS clip-on extensometer was used to measure total axial strain, ε. Total engineering shear strain, γ, was acquired by four precision strain gages attached to the gage section of the specimen. Axial stress, σ, and shear stress, τ, were calculated from load and torque data measured with an axial–torsional load cell. Both UFG and CG nickel specimens were subjected to identical cyclic straining experiments as follows:

1. Constant amplitude: $\varepsilon_{pa,eff} = 1 \times 10^{-4}$, proportional.
2. Constant amplitude: $\varepsilon_{pa,eff} = 1 \times 10^{-4}$, non-proportional.
3. Constant amplitude: $\varepsilon_{pa,eff} = 1 \times 10^{-3}$, proportional.
4. Constant amplitude: $\varepsilon_{pa,eff} = 1 \times 10^{-3}$, non-proportional.
5. Multiple step test at $\varepsilon_{pa,eff}$ ranging from 1×10^{-4} to 1×10^{-3}, proportional.
6. Multiple step test at $\varepsilon_{pa,eff}$ ranging from 1×10^{-4} to 1×10^{-3}, non-proportional.

The effective plastic strain amplitude, $\varepsilon_{pa,eff}$, is defined as the radius of the circle that circumscribes the loading path in plastic strain space $(\varepsilon_p - \gamma_p/\sqrt{3})$ [14]. For proportional straining, $\varepsilon_{pa,eff} = (\varepsilon_{pa}^2 + \gamma_{pa}^2/3)^{1/2}$, where ε_{pa}

and γ_{pa} are the axial and engineering shear plastic strain amplitudes, respectively. For the non-proportional straining used in this study, we approximate the radius of the circular loading path as $\varepsilon_{pa,eff} = (\varepsilon_{pa} + \gamma_{pa}/\sqrt{3})/2$. During all the tests, cycling continued until the stress amplitudes had clearly saturated as evidenced by either a peak in the cyclic hardening curve or a plateau that lasted at least 2000 cycles at the lower $\varepsilon_{pa,eff}$ or 200 cycles at the higher $\varepsilon_{pa,eff}$.

Typical imposed strain paths and responses at cyclic saturation for the UFG specimen cycled at $\varepsilon_{pa,eff} = 1 \times 10^{-3}$ are shown in Figures 1–3. In Figure 1, normalized total shear strain, $\gamma/\sqrt{3}$, is plotted versus total axial strain, ε. For the proportional case shown in Figure 1, the amplitudes of the two strain components are equal and in-phase thus producing the 45° line strain path in $\varepsilon - \gamma/\sqrt{3}$ space. For the non-proportional case, the amplitudes of the shear and axial strain components are approximately equal, but 90° out-of-phase causing the circular strain path. The normalized shear stress, $\sqrt{3}\tau$, versus axial stress, σ, responses are shown in Figure 2. These responses parallel the imposed strain
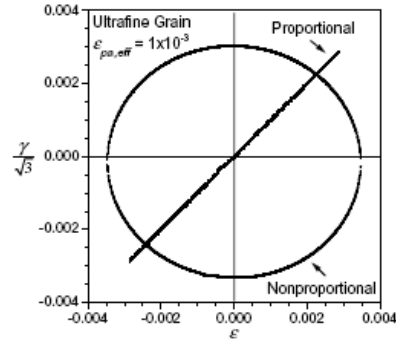

Figure 1. Total normalized shear strain, $\gamma/\sqrt{3}$, versus total axial strain, ε, for proportional and non-proportional cycling of ultrafine grain nickel at $\varepsilon_{pa,eff} = 1 \times 10^{-3}$.
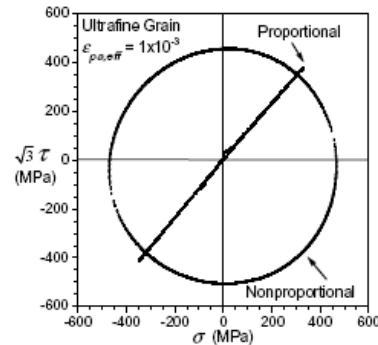

Figure 2. Normalized shear stress, $\sqrt{3}\tau$, versus axial stress, σ, for proportional and non-proportional cycling of ultrafine grain nickel at $\varepsilon_{pa,eff} = 1 \times 10^{-3}$.

paths quite closely. The resulting plastic strain responses are shown in Figure 3 where normalized plastic shear strain, $\gamma_p/\sqrt{3}$, is plotted versus axial plastic strain, ε_p. Here, $\gamma_p = \gamma - \tau/G$ and $\varepsilon_p = \varepsilon - \sigma/E$. The Young's modulus, E, and shear modulus, G, for the CG material were approximately 200 and 70 GPa, respectively. For the UFG nickel, the E and the G were approximately 165 and 60 GPa, respectively. The lower moduli for the UFG nickel may be caused by the strong $\langle 100 \rangle$ radial texture [15]. In addition, the small amount of porosity commonly seen in electrodeposited nickel may cause a modulus reduction [16]. Molecular dynamics simulations predict that grain size will not have a significant effect on modulus unless the grain size is less than 10 nm [17].

Response plots similar to those shown in Figures 1–3 were produced for the UFG and CG nickel cyclically saturated under all the test conditions listed previously. From these plots, the cyclic stress–strain (CSS) curves shown in Figure 4 were constructed. The CSS curves show the effects that imposed effective plastic strain amplitude have on the saturation effective stress amplitude, $\sigma_{sa,eff}$. Effective stress amplitude is defined as the radius of the circle that circumscribes the loading path in stress space $(\sigma - \sqrt{3}\tau)$. For proportional loading, $\sigma_{sa,eff} = (\sigma_{sa}^2 + 3\tau_{sa}^2)^{1/2}$, where σ_{sa} and τ_{sa} are the axial and shear stress amplitudes at cyclic saturation. For the non-proportional loading path used in this study, $\sigma_{sa,eff} = (\sigma_{sa} + \sqrt{3}\tau_{sa})/2$.

The CG nickel CSS curves are shown in Figure 4a. The response of the CG nickel subjected to the proportional strain path is quite similar to uniaxial results on untextured CG nickel reported by Morrison and Chopra [18]. This result is expected because the orientation of the principal strain axes remains fixed during both types of cycling. On the other hand, the non-proportional strain path used in this study causes the orientation of the principal strain axes to continually rotate. As a result, multiple slip systems are activated. The multiple slip enhances dislocation interactions and usually causes additional cyclic hardening compared with proportional straining at the same effective plastic strain amplitude [19]. As shown in Figure 4a, at $\varepsilon_{pa,eff} \approx$
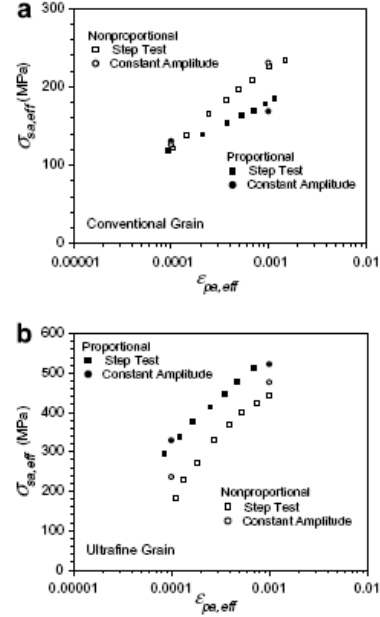
Figure 4. Effective cyclic stress–strain curves for: (a) conventional grain and (b) ultrafine grain nickel.

1×10^{-3}, the non-proportional strain path causes an approximately 28% increase in the saturation effective stress amplitude. This degree of additional hardening compares favorably with the value of 27% reported by Itoh et al. [20] for CG nickel tested at $\varepsilon_{pa,eff} \approx 1 \times 10^{-3}$. As effective plastic strain amplitude decreases to 1×10^{-4}, the additional hardening caused by non-proportional straining diminishes to almost zero. Zhang and Jiang [21] also noted a reduction of the additional hardening in CG copper as effective plastic strain decreases. However, Doong et al. [22] observed the opposite effect in CG copper and found that the additional hardening increases as effective plastic strain amplitude decreases. A decrease in additional hardening as effective plastic strain amplitude decreases is commonly seen in austenitic stainless steels [22].

The CSS response of the UFG nickel is shown in Figure 4b. Clearly the UFG nickel saturates at significantly higher effective stress amplitudes than the CG nickel. In addition to grain refinement, differences in texture and impurity level could affect the CSS responses. The $\langle 100 \rangle$ radial texture of the UFG nickel is rotationally symmetric about the radial direction. Hosford and Backofen [23] analyzed the mechanical behavior of sheet metal with $\langle 100 \rangle$ texture normal to the plane of the sheet and rotationally symmetric texture in the plane of the sheet. For uniaxial loading along directions in the plane of the sheet, the Taylor factor [24] was calculated to be less than the 3.06 value of randomly oriented grains, which indicates that these are "soft" directions. Sheet metal directions in the plane of the sheet correspond to directions in the tubular axial–torsional specimen perpendicular to the radial direction. These are the
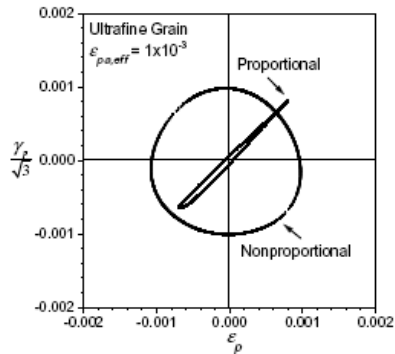

Figure 3. Normalized plastic shear strain, $\gamma_p/\sqrt{3}$ versus plastic axial strain, ε_p, for proportional and non-proportional cycling of ultrafine grain nickel at $\varepsilon_{pa,eff} = 1 \times 10^{-3}$.

directions in which the principal stresses act. Although one could question the applicability of the Taylor model to UFG cyclic plasticity, and texture effects are sensitive to the biaxial stress state [23], based on the current understanding of UFG deformation mechanisms, it is reasonable to conclude that the influence of texture on the CSS response is not significant, especially when comparing the responses under similar strain paths. Although the UFG material has a higher impurity level than the CG nickel, Mughrabi and Wang [25] showed that low levels of impurities do not significantly affect the CSS response. Therefore, the differences in the UFG and CG hardening under similar strain paths would seem to be primarily associated with grain refinement.

Figure 4b shows that the UFG nickel exhibits increased hardening under proportional straining compared with the non-proportional case. This behavior is quite unusual. There are some materials such as pure aluminum that exhibit the same hardening under proportional and non-proportional straining [22] owing to a very high stacking fault energy that causes similar dislocation structures to form under both types of strain paths [26,27]. It is known that fundamental plasticity mechanisms in UFG materials are different from those that govern the response of CG materials [1,2]. The effects of the UFG radial texture could be sensitive to the stress states induced by the different strain paths. Transmission electron microscopy studies are currently being performed to provide insight into these fundamental mechanisms and to relate them to the UFG multiaxial response. Another factor that could influence the results is the inherent difficulty in producing electrodeposited UFG materials with consistent mechanical properties from specimen to specimen [28]. In an attempt to minimize this possibility, hardness measurements were obtained from the electrodeposited tubes prior to machining; and all the specimens used in the study had similar hardness values.

From the results of this study, the following conclusions can be made:

1. Under the cyclic biaxial straining conditions used in this study, ultrafine grain nickel exhibits significantly higher saturation effective stress amplitudes than conventional grain nickel.
2. In conventional grain nickel, the additional cyclic hardening associated with non-proportional straining is negligible at $\varepsilon_{pa,eff} = 1 \times 10^{-4}$ but increases as effective plastic strain amplitude increases. At $\varepsilon_{pa,eff} = 1 \times 10^{-3}$, the non-proportional strain path increases the saturation effective stress amplitude by about 28%.
3. In the ultrafine grain nickel examined in this study, non-proportional straining results in a reduction of the saturation effective stress amplitude compared with the proportional case.

[1] M.A. Meyers, A. Mishra, D.J. Benson, Prog. Mater. Sci. 51 (2006) 427.
[2] K.S. Kumar, H. Van Swygenhoven, S. Suresh, Acta Mater. 51 (2003) 5743.
[3] R.Z. Valiev, R.K. Islamgaliev, I.V. Alexandrov, Prog. Mater. Sci. 45 (2000) 103.
[4] A. Vinogradov, Y. Kaneko, K. Kitagawa, S. Hashimoto, V. Stolyarov, R. Valiev, Scripta Mater. 36 (1997) 1345.
[5] S.R. Agnew, J.R. Wertman, Mater. Sci. Eng. A 244 (1998) 145.
[6] A. Vinogradov, V.V. Stolyarov, S. Hashimoto, R.Z. Valiev, Mater. Sci. Eng. A 318 (2001) 163.
[7] H.W. Hoppel, M. Kautz, C. Xu, M. Murashkin, T.G. Langdon, R.Z. Valiev, H. Mughrabi, Int. J. Fatigue 28 (2006) 1001.
[8] L. Kunz, P. Lukas, M. Svoboda, Mater. Sci. Eng. A 424 (2006) 97.
[9] H.J. Maier, P. Gabor, N. Gupta, I. Karaman, M. Haouaoui, Int. J. Fatigue 28 (2006) 243.
[10] T. Hanlon, E.D. Tabachnikova, S. Suresh, Int. J. Fatigue 27 (2005) 1147.
[11] E. Thiele, R. Klemm, L. Hollang, C. Holste, N. Schell, H. Natter, R. Hempelmann, Mater. Sci. Eng. A 390 (2005) 42.
[12] B. Moser, T. Hanlon, K.S. Kumar, S. Suresh, Scripta Mater. 54 (2006) 1151.
[13] J. Xie, X. Wu, Y. Hong, Scripta Mater. 57 (2007) 5.
[14] Y. Jiang, P. Kurath, Int. J. Plasticity 13 (1997) 743.
[15] K.J. Hemker, H. Last, Mater. Sci. Eng. A 319–321 (2001) 882.
[16] H.S. Cho, K.J. Hemker, K. Lian, J. Goettert, G. Dirras, Sensor Actuat. A 103 (2003) 59.
[17] J.R. Weertman, D. Farkas, K. Hemker, H. Kung, M. Mayo, R. Mitra, H. Van Swygenhoven, MRS Bull. 24 (2) (1999) 44.
[18] D.J. Morrison, V. Chopra, Mater. Sci. Eng. A 177 (1994) 29.
[19] H.S. Lamba, O.M. Sidebottom, ASME J. Eng. Mater. Technol. 100 (1978) 96.
[20] T. Itoh, M. Sakane, M. Ohnami, K. Ameyama, in: Proceedings of Mecamat 92, International Seminar on Multiaxial Plasticity, LMT-Cachan, France, 1992, pp. 43–50.
[21] J. Zhang, Y. Jiang, Int. J. Plasticity 21 (2005) 2191.
[22] S.H. Doong, D.F. Socie, I.M. Robertson, ASME J. Eng. Mater. Technol. 112 (1990) 456.
[23] W.F. Hosford, W.A. Backofen, in: W.A. Backofen, J.J. Burke, L.F. Coffin, N.L. Reed, V. Weiss (Eds.), Fundamentals of Deformation Processing, Syracuse University Press, Syracuse, NY, 1964, pp. 259–292.
[24] G.I. Taylor, J. Inst. Met. 62 (1938) 307.
[25] H. Mughrabi, R. Wang, in: P. Lukas, J. Polak (Eds.), Basic Mechanisms in Fatigue of Metals, Elsevier, Amsterdam, 1988, pp. 1–13.
[26] M. Clavel, X. Feaugas, in: A. Pineau, G. Cailletaud, T.C. Lindley (Eds.), Multiaxial Fatigue and Design, Mechanical Engineering Publications, London, 1996, pp. 21–41.
[27] M.V. Borodii, S.M. Shukaev, Int. J. Fatigue 29 (2007) 1184.
[28] F. Dalla Torre, H. Van Swygenhoven, M. Victoria, Acta Mater. 50 (2002) 3957.